PHYSICAL REVIEW B **73**, 115319 (2006)

Quantum confinement induced by strain relaxation in an elliptical double-barrier Si/Si$_x$Ge$_{1-x}$ resonant tunneling quantum dot

Guohua Wang
Department of Physics, Brown University, Providence, Rhode Island 02912, USA

D. T. Tambe, A. Zaslavsky, and V. B. Shenoy
Division of Engineering, Brown University, Providence, Rhode Island 02912, USA

(Received 12 October 2005; revised manuscript received 20 December 2005; published 16 March 2006)

Starting with a double-barrier p-Si/Si$_{0.75}$Ge$_{0.25}$ resonant tunneling heterostructure, we fabricated sub-100-nm elliptical quantum dots. Sidewall strain relaxation in the Si$_x$Ge$_{1-x}$ layer induces a lateral confining potential that quantizes heavy hole (HH) and light hole (LH) states in the SiGe quantum well, leading to fine structure in the HH-LH $I(V)$ resonant tunneling curves at low temperature. In this paper, we present the magnetotunneling $I(V,B)$ characteristics of heavy holes and light holes in magnetic fields B parallel to the tunneling current. From the evolution of the fine structure, we observe the competition between the strain-induced lateral confinement potential and the magnetic confinement, from which we infer lateral potentials of HH and LH different from those of previously studied cylindrically symmetric dots. The experimental data are in qualitative agreement with inhomogeneous strain-induced HH and LH potential obtained via a full three-dimensional finite-element strain simulation.

DOI: 10.1103/PhysRevB.73.115319 PACS number(s): 73.40.Gk, 73.21.La

I. INTRODUCTION

Advances in microfabrication techniques have made it possible to fabricate deep submicrometer double-barrier resonant tunneling (RT) diodes exhibiting lateral quantization and three-dimensionally confined states in the quantum well. Lateral quantization was first observed in small III–V quantum dots,[1–3] where the lateral potential is determined by the Fermi level pinning at the GaAs surface. In the Si/Si$_x$Ge$_{1-x}$ RT diodes we have been studying, the lateral surface is passivated with SiO$_2$, but an additional source of lateral potential arises from inhomogeneous strain in the Si$_x$Ge$_{1-x}$ layers.

In large devices, the lattice mismatch between Si and Si$_x$Ge$_{1-x}$ introduces biaxial strain, and as long as the strained Si$_x$Ge$_{1-x}$ layer thickness is kept below the critical thickness h_C,[4] the Si$_x$Ge$_{1-x}$ remains homogeneously strained. The strain lifts the degeneracy of the heavy-hole (HH) and light-hole (LH) valence band and reshapes the HH and LH dispersions.[5] When a quantum dot or wire is etched out of the strained Si/Si$_x$Ge$_{1-x}$ heterostructure, the biaxial strain can relax by sidewall expansion. This has been demonstrated by Raman spectroscopy[6] and resonant tunneling measurements.[7–9] Since the HH-LH subband energy separation contains a large strain-induced contribution,[5] the HH and LH peak spacing is an experimentally accessible indication of the strain in the structure. As the lateral size of the structures decreases, an unambiguous reduction of the HH-LH energy separation corresponding to strain relaxation has been observed.[7,8] As the size of the dot is reduced further, additional fine structure is observed in the HH and LH resonant peaks, consistent with lateral quantization due to nonuniform strain.[8,9] The HH fine structure is generally stronger, because the states arising from the HH subband have a lighter in-plane mass[5] and hence are more strongly quantized by the lateral inhomogeneous strain-induced potential. The observed changes in the HH $I(V)$ peak have been compared to a finite-element simulation of the strain and its effect on the electronic states in a cylindrically symmetric quantum dot.[8,10] The radially symmetric two-dimensional simulations[10] predicted nonmonotonic radial strain distributions, and in sufficiently small quantum dots, the confinement of the ground state is a ringlike region around the perimeter. This surprising prediction was consistent with the subsequently observed ϕ/ϕ_0 periodicity of fine structure in the RT peaks in small magnetic fields (where ϕ is the enclosed magnetic flux and $\phi_0=h/e$ is the flux quantum), the signature of a quantum ring.[11]

Since strain relaxation is determined not only by the size, but also by the geometry, we have fabricated sub-100-nm elliptical quantum dots to investigate the resulting strain-induced lateral potential by observing the fine structure in the HH and LH RT $I(V)$ peaks and their evolution in magnetic fields B parallel to the tunneling direction. We observe partial quenching of the fine structure by $B>5$ T that is consistent with the competition between the strain-relaxation-induced lateral potential confinement and magnetic confinement. Unlike the cylindrical quantum dots, we do not observe magnetic flux periodicity in the HH $I(V)$ fine structure. Carrying out a full three-dimensional simulation of the strain relaxation in elliptical quantum dots, we get a strain relaxation that is different from that of the cylindrical quantum dot. The potential induced by this elliptical strain relaxation does not confine the ground state of the HH and LH to a ring around the perimeter, providing a qualitative explanation for the absence of the quantum ring signature in the HH $I(V)$ data. Our numerical analysis of the density of states in the elliptical dot with and without B is consistent with the observed partial quenching of the $I(V)$ fine structure.

II. EXPERIMENTAL TUNNELING RESULTS IN THE ELLIPTICAL QUANTUM DOT WITHOUT MAGNETIC FIELD

The submicrometer elliptical quantum dot we measured was fabricated from strained p-Si/Si$_x$Ge$_{1-x}$ double-barrier RT material.[8] The nominally undoped double-barrier active region consists of a 35 Å Si$_{0.75}$Ge$_{0.25}$ quantum well confined by two 50 Å Si barriers. On both sides of the double-barrier region, there are 100 Å undoped Si$_{0.75}$Ge$_{0.25}$ spacer layers, followed by 100 Å regions in which the Ge content is linearly graded to zero. The doping is turned off (on) in the middle of these graded regions below (above) the active region, leading to nominally symmetric undoped 150 Å material on both sides of the structure. However, due to the unintentional diffusion of dopants with the growth front, the real undoped spacer on the substrate side is expected to be smaller than on the top. Electron-beam lithography was used to define the elliptical Ti/Al top contact of the dot, and reactive ion etching was utilized to fabricate a deep submicrometer pillar, followed by SiO$_2$ passivation, polishing, etch back, and deposition of the large contact pad.

The $I(V)$ characteristics of a large device (nominal diameter $D=1.5$ μm) measured at $T=1.7$ K and $B=0$ are shown in Fig. 1(a). In this large device, we observe smooth RT current peaks corresponding to the usual resonant tunneling into two-dimensional subbands arising from the heavy-hole and light-hole branches of the dispersion.[12] Given the double-barrier heterostructure parameters, a self-consistent calculation of the potential distribution over the device was used to convert the applied bias V to the alignment of the occupied emitter states with the subbands in the quantum well. A complete self-consistent conversion must take into account the formation of the accumulation and depletion layers in the emitter and collector electrodes, including the potential drop over the undoped spacer region in the collector electrode (as well as the space charge in the well created by the tunneling carriers).[13,14] Given a calculation of the HH and LH two-dimensional (2D) subbands in the SiGe quantum well, the expected bias positions of the threshold V_T and peak V_p of the HH and LH RT resonances can be determined from E and $k_\perp$ conservation:[15] V_T occurs when the HH or LH subband aligns with E_F in the emitter, V_p occurs when HH or LH approximately aligns with the valence band edge in the emitter valence band. Figure 1(b) shows the HH and LH 2D subband energies and their in-plane dispersions in our Si$_x$Ge$_{1-x}$ quantum well, referred to the Fermi level E_F in the emitter at zero bias. The calculation is shown for both full biaxial strain [corresponding to large structures, such as the $D=1.5$ μm device of Fig. 1(a)] and partially relaxed strain (which will be needed later, when we discuss the small elliptical quantum dot). The 6×6 effective-mass Hamiltonian used for the calculation,[16–19] includes directional anisotropy, leading to different in-plane dispersions in $\langle 10\rangle$ and $\langle 11\rangle$ directions. The strong nonparabolicity and anisotropy predicted by the calculated dispersion curves in Si$_x$Ge$_{1-x}$ quantum wells have been observed experimentally for large $k_\perp$.[20] By combining the self-consistent potential distributions with the HH and LH 2D energy subbands calculations at full strain of Fig. 1(b), we obtain the calculated V_T and V_P positions for the RT tunneling peaks in both polarities, superimposed on the data in Fig. 1(a). The calculation assumes full strain in the Si$_x$Ge$_{1-x}$ well and the slight asymmetry in the undoped spacer layers, due to the unintentional dopant migration mentioned previously. The agreement with the measured RT peak positions is very good, confirming the accuracy of the self-consistent conversion of applied bias V to subband energy in the quantum well. The experimentally observed asymmetry in the RT peak current magnitudes at positive and negative bias is likely due to a slight unintentional asymmetry in the Si barrier thicknesses. Since the transmission coefficient is exponentially dependent on the barrier thickness, taking the emitter barrier to be 50 Å, as designed and assuming the collector barrier to be slightly thicker at 55 Å leads to the HH peak current ratio of $\sim 1/3$ in the positive vs negative bias polarity, similar to the measured $I(V)$.

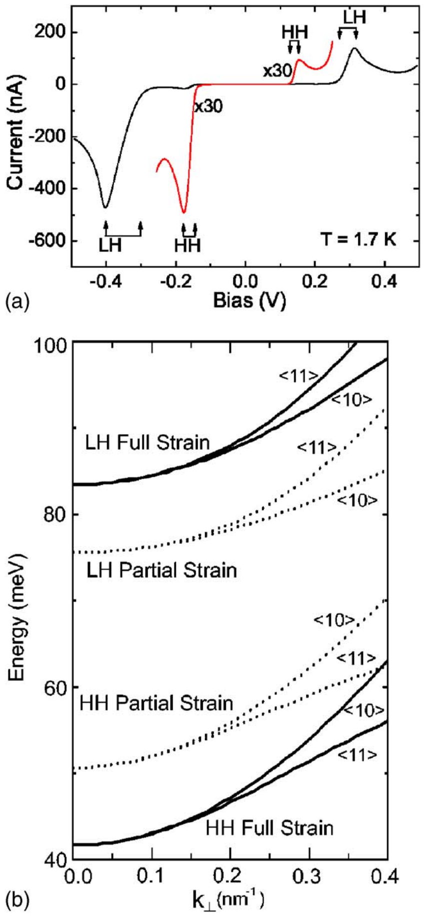

FIG. 1. (Color online) (a) Smooth $I(V)$ characteristics of a large device with diameter $D=1.5$ μm for both bias polarities. Arrows show the calculated threshold and peak bias values for the HH and LH peaks in both polarities. (b) Calculated HH and LH subbands $E(k_\perp)$ dispersion at full strain ($\varepsilon=-1$) and partially relaxed strain ($\varepsilon=-0.4$), corresponding to 60% strain relaxation, in the Si$_x$Ge$_{1-x}$ quantum well. The energy is referred to the Fermi level E_F in the emitter.

Figure 2(a) shows the scanning electron microscope (SEM) micrograph of the Ti/Al top contact of the elliptical quantum dot under study. The long axis is about 80 nm, and

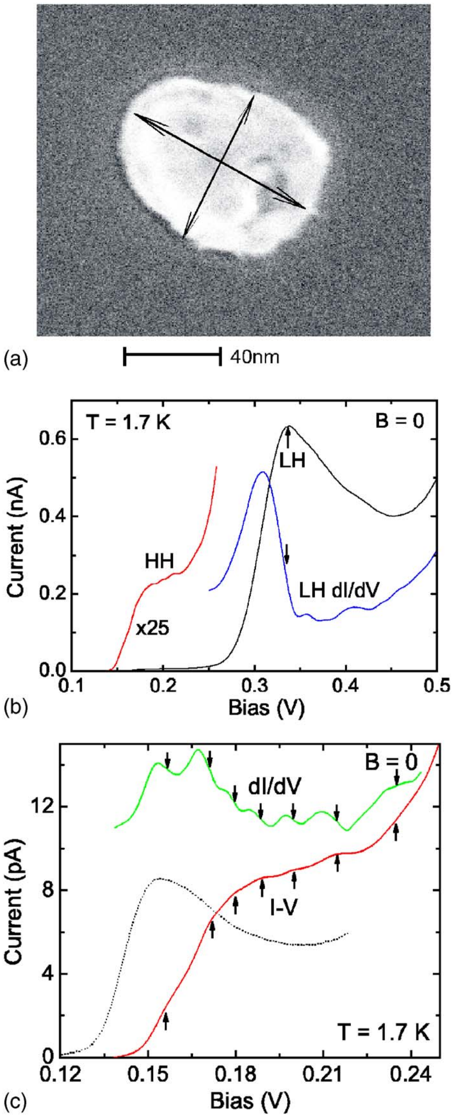

FIG. 2. (Color online) (a) SEM top contact micrograph of the elliptical quantum dot under study; long axis is ~80 nm, short axis is ~60 nm. (b) HH and LH $I(V)$ tunneling peaks of the elliptical quantum dot at $B=0$ and $T=1.7$ K, together with expanded $(25\times)$ views of the HH peak and the dI/dV characteristics of the LH peak. Arrows are used to point out the position of the LH peak in the $I(V)$ and dI/dV characteristics. (c) Expanded view of the HH $I(V)$ peak, and the corresponding dI/dV characteristics; arrows used to point out the fine structure features. For comparison, the smooth HH $I(V)$ peak of the large $D=1.5$ μm device of Fig. 1(a) is also shown (dotted line).

short axis is about 60 nm. The geometry of the dot was made intentionally elliptic by exposing two adjacent circular dots in close proximity. Although the pillar etching process does not produce perfectly vertical sidewalls, previous work[8] has shown that the shape and size of the top contact are reproduced quite closely in the active region. The HH-LH $I(V)$ curve of this small elliptical dot measured at $T=1.7$ K and $B=0$ is shown in Fig. 2(b). Both the HH and LH peaks have acquired a fine structure. The fine structure in the LH peak is weaker, so the corresponding dI/dV characteristic of the LH peak is also shown. Since the LH peak lineshape is still fairly similar to the smooth $I(V)$ of the large device in Fig. 1(a), we can compare the currents and corroborate the diameter of smaller dot—we obtain an approximate diameter of ~100 nm, in reasonable agreement with Fig. 2(a) given that strain relaxation alters the effective tunneling barrier heights,[5,7] and exact current scaling with area cannot be expected in the deep submicrometer regime.

The observed fine structure remains essentially unchanged if the temperature is raised to $T=4.2$ K, but is completely quenched at $T=77$ K as the thermal broadening becomes larger than the energy separations of the confined HH in-plane states. In order to minimize thermal broadening, all measurements were carried out at $T=1.7$ K. Also, since the aim of this paper is to examine the effects of noncylindrical geometry on strain relaxation as evidenced by the fine structure, we will first focus on the HH peak, where the fine structure is stronger, although data on LH peak will also be shown and analyzed.

An expanded view of the HH $I(V)$ characteristics is shown in Fig. 2(c), together with the corresponding dI/dV characteristics. The fine structure features, shown by arrows, are obtained by finding the steepest descending slopes in the dI/dV characteristics. We also plot the scaled HH $I(V)$ curve of the large device shown in Fig. 1(a) for comparison. Compared with the smooth HH peak of the large device, the threshold V_T has been shifted to higher bias, as expected from strain relaxation in the Si_xGe_{1-x} quantum well.[7–10] The fine structure is quasiperiodic with a period of ~10 mV, corresponding to ~2.5 meV in energy using a self-consistent calculation of potential distribution over the active region. Previous work on cylindrically symmetric submicron RT dots from the same Si/Si_xGe_{1-x} material correlated this fine structure with lateral quantization due to inhomogeneous-strain-induced potential.[8,10,11] In order to analyze this quasiperiodic structure in this elliptical quantum dot, we used the finite-element method in three dimensions to simulate the corresponding potential profile in the quantum well, as described in the next section.

III. STRAIN SIMULATION OF THE ELLIPTICAL QUANTUM DOT BY FINITE-ELEMENT METHOD

Unlike the cylindrically symmetric quantum dots simulated previously,[10] the elliptical quantum dot requires a full 3D strain simulation.[21] Since the Ge content of the Si_xGe_{1-x} layers used for our fabrication is nominally symmetric about the midplane of the quantum well, only half of the structure is modeled, as shown in Fig. 3(a), where the composition profile of Ge in different layers is also shown. The cross-section of the simulated pillar closely resembles the top contact SEM picture of the dot, as shown in Fig. 2(a). The mesh near the peripheral regions of barrier and well layers is refined, as large strain gradients are expected in those regions. The simulated remaining strain in the quantum well is shown in Fig. 3(b), while the cross-sectional views of remaining radial strain in the quantum well in X and Y directions are shown in Fig. 3(c).

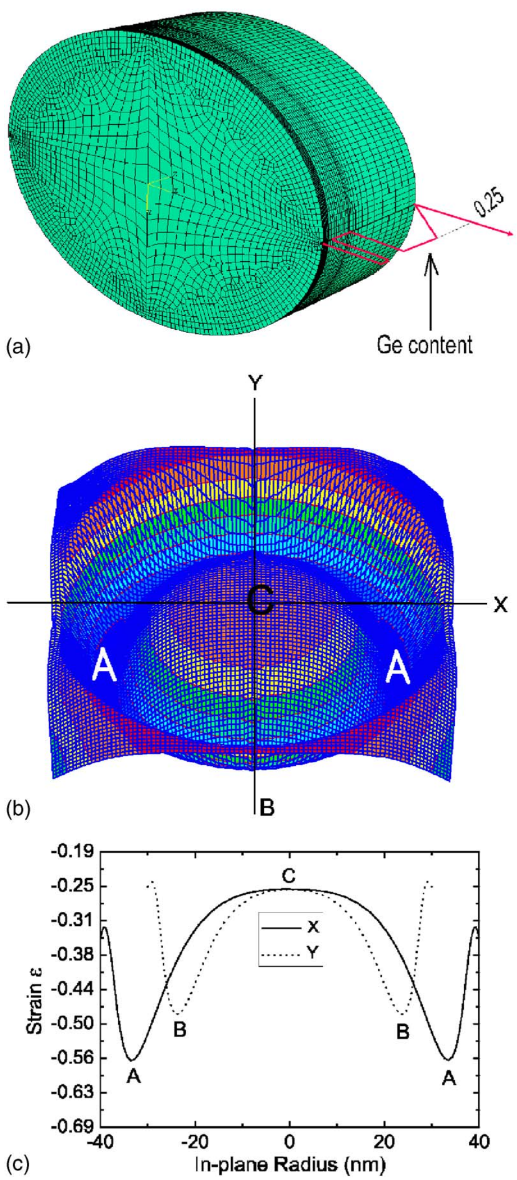

FIG. 3. (Color online) (a) Model used to simulate the strain relaxation in our quantum dot; only half of the structure is simulated due to Ge content symmetry about the midplane of the SiGe quantum well. (b) Strain profile by finite element simulation. In our notation, full biaxial strain corresponds to $\varepsilon \equiv -1$, fully relaxed strain is $\varepsilon \equiv 0$. Regions A are the most strained regions; B is the bottom of the ringlike region; C is the least strained region. (c) Cross sections of the partially relaxed strain in the quantum well in X and Y directions; points A, B, C are the same as in (b).

We estimate the in-plane confining potential for HH and LH states by retaining only the radial ε_{xx} and ε_{yy} components that are most affected by strain relaxation (in previous cylindrically symmetric dot simulations,[8,10,11] we retained only the radial component ε_{rr}). Strain relaxation in the quantum well cannot only reduce the separation between the HH and LH subbands in the quantum well, which has been demonstrated by experiment,[7] but also increase the band gap E_G,[5] hence affecting the valence band edge. These two effects have been taken into account as follows. First, we calculate the HH subband energy at $k_\perp = 0$ as a function of local strain ε_{xx} and ε_{yy} by the usual six-band Luttinger-Kohn Hamiltonian.[22] Second, since we know the energy separation between HH and LH at each different local strain, based on the calculated potential of HH, we can get the LH potential by adding the energy separation to the HH potential. The calculated potentials of HH and LH are shown in Fig. 4 for two cross-sectional cuts through the elliptical dot. The zero-point energy corresponds to the Fermi level E_F in the emitter, where the strain relaxation is also taken from the finite-element simulation. (Since the strain relaxes by sidewall expansion, the strained Si_xGe_{1-x} layers relax more in the quantum well than in the emitter. We approximate the average strain relaxation in the emitter by 80% that of the well, a value consistent with the calculated strain relaxation ~100 Å into the emitter.) From Figs. 3(b), 3(c), and 4, we find that regions marked as A in Fig. 3(c), lying toward the perimeter along the longer axis of the elliptical dot, are the lowest potential regions for both heavy holes and light holes. Taking the coordinates of the potential minimum in region A as (x_0, y_0), as a first approximation we can use asymmetric parabolic confinement in both directions to describe region A. Above region A, which confines the ground state of the lateral potential, we have a ringlike potential along the perimeter going through the minimum B (along the shorter axis of the ellipse), whereas region C in the middle of the elliptical dot corresponds to a potential hill—see Fig. 3(b). The calculated energy difference between the HH potential minimum points of regions A and B is ~8 meV, due to the geometrical asymmetry of the elliptical dot. From this simulation, we see that the ground state is confined to regions A on the opposite sides of the long axis of the ellipse.

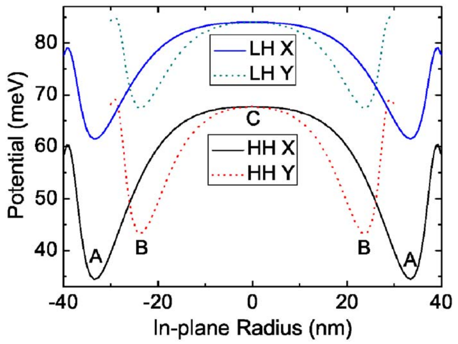

FIG. 4. (Color online) By retaining only the radial ε_{xx} and ε_{yy} components that are most affected by strain relaxation, calculated HH and LH potential energies in the quantum well in X and Y directions using the six-band Luttinger-Kohn Hamiltonian are shown here. Points A, B, C are the same as in Figs. 3(b) and 3(c).

IV. CHARACTERIZATION OF THE STRAIN CONFINEMENT BY MAGNETOTUNNELING MEASUREMENTS

Previously, in cylindrically symmetric quantum dots, the calculated inhomogeneous strain relaxation confined the HH ground state to a quantum ring near the perimeter of the device. Measurements of the HH peak fine structure in cylindrically symmetric dots revealed a ϕ/ϕ_0 periodicity in the energy of the fine structure features, where ϕ is the magnetic flux enclosed in the ringlike orbit.[11] Since the area of this small elliptical quantum dot is known from Fig. 2(a), a similar confinement of the ground state to the perimeter of the elliptical dot would result in a periodicity of ~ 1 T. We measured the HH $I(V)$ characteristics under constant magnetic field $B=0-3$ T with a step 0.1 T, small enough to resolve such periodicity. No ϕ/ϕ_0 periodicity of the fine structure is observed. This is consistent with the confining potential due to inhomogeneous strain relaxation in the elliptical quantum, shown in Fig. 4. Unlike in the cylindrical quantum dot,[11] the ~ 8 meV potential difference between minima A and B interrupts the ringlike ground state around the perimeter. Due to the interruption, holes will be scattered into fully confined region A, preventing 1D quantum ring behavior (like the ϕ/ϕ_0 periodicity in magnetotunneling spectroscopy that has been observed in cylindrical quantum dots).[11]

The HH $I(V,B)$ curves in higher magnetic fields B parallel to the tunneling direction z are shown separately in Figs. 5(a) and 5(b) for positive and negative bias polarities. In both polarities $I(V,B)$ characteristics with different B up to 10 T have been shifted for clarity. The HH fine structure peak positions of the positive polarity plotted against B are shown in Fig. 5(c). We find that in both bias polarities, when B is increased above approximately 5 T, the fine structure is partially quenched: the number of fine structure peaks is reduced and some peaks tend to merge into each other. When $B=10$ T, the remaining fine structure is still quasiperiodic, but with a much bigger period of ~ 20 mV in bias, corresponding to ~ 5 meV in energy.

Another experimental check on the potential induced by the strain relaxation in the quantum well is available by doing magnetotunneling experiments on fine structure superimposed on the LH resonant tunneling peak, as shown in Fig. 6(a). The corresponding dI/dV characteristics are shown in Fig. 6(b). From this figure, we can see that as B is increased beyond 5 T, some fine structure has been quenched, which is similar to the HH fine structure changing with B. Since the LH confining potential induced by the strain relaxation in the quantum well is similar to the HH potential, as shown in Fig. 4, it is not surprising that similar fine structure quenching at high magnetic field is observed.

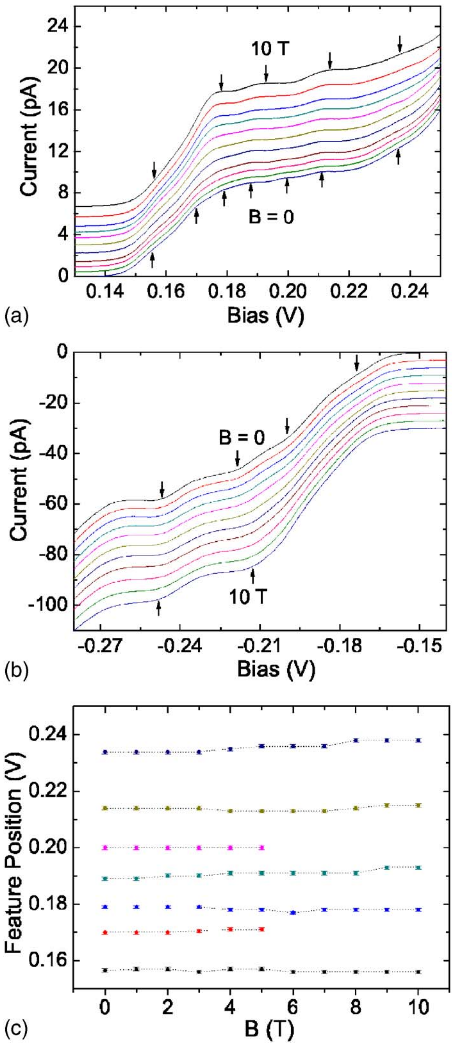

FIG. 5. (Color online) HH $I(V,B)$ characteristics of elliptical quantum dot in forward bias (a) and reverse bias (b) under constant B from 0 to 10 T with step 1 T parallel to the current. The $I(V)$ curves with different magnetic fields are offset vertically for clarity; arrows are used to point out the fine structure positions. HH fine structure positions in positive bias polarity are plotted against B in (c).

V. CALCULATION OF DENSITY OF STATES IN THE WELL IN THE PRESENCE OF STRAIN RELAXATION AND MAGNETIC FIELD

We explain the merging of peaks and increased fine structure period in high B by the interplay of the strain-induced lateral confinement of Fig. 3(c) and the magnetic confinement. As a first-order approximation, which allows for the use of analytic solutions,[23,24] we will treat the lateral confining potential of region A as parabolic, but with different force constants corresponding to motion along long (X) and short (Y) axes of the ellipse:

$$V(r)=\frac{1}{2}m^*\omega_1^2(x-x_0)^2+\frac{1}{2}m^*\omega_2^2(y-y_0)^2 \tag{1}$$

where (x_0,y_0) is the potential minimum point of region A, shown in Fig. 4. Under magnetic field in the z direction, choosing a gauge such that vector potential $A=(0,Bx,0)$, the Hamiltonian H in the plane becomes

$$H=\frac{1}{2m^*}\{p_x^2+[p_y+eB(x-x_0)]^2\}+\frac{1}{2}m^*\omega_1^2(x-x_0)^2+\frac{1}{2}m^*\omega_2^2(y-y_0)^2. \tag{2}$$

The resulting eigenenergies are given by[23,24]

$$E_{ij}=\hbar\omega_+\left(i+\frac{1}{2}\right)+\hbar\omega_-\left(j+\frac{1}{2}\right) \tag{3}$$

where

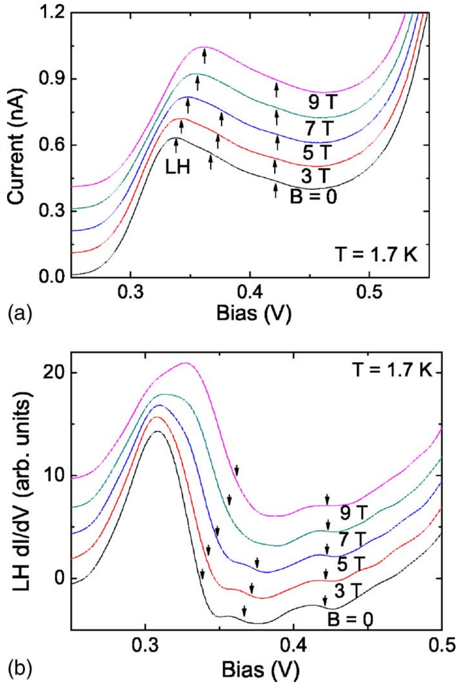

FIG. 6. (Color online) (a) LH $I(V,B)$ characteristics of elliptical quantum dot in forward bias under constant B parallel to the current. The $I(V)$ curves with different magnetic fields are offset vertically for clarity; arrows are used to point out the superimposed fine structure positions. (b) The corresponding dI/dV characteristics are plotted.

$$2\omega_\pm^2 = \omega_1^2 + \omega_2^2 + \omega_c^2 \pm [(\omega_1^2 - \omega_2^2 + \omega_c^2)^2 + 4\omega_2^2\omega_c^2]^{1/2}. \tag{4}$$

The magnetization exhibits the superposition of large-period ($\hbar\omega_+$) and small-period ($\hbar\omega_-$) oscillations. We take the in-plane effective masses that enter into Eqs. (1)–(4) from the $k_\perp=0$ solutions of the 6×6 effective-mass Hamiltonian in Fig. 1(b),[16–19] taking an averaged strain $\varepsilon=-0.4$ in the quantum well according to the strain distribution shown in Fig. 3(c). The resulting in-plane effective masses for HH and LH subbands are $m^*=0.26m_0$ and $m^*=0.55m_0$, respectively. For the HH, we have $\hbar\omega_1\sim 8$ meV and $\hbar\omega_2\sim 2.5$ meV, whereas $\hbar\omega_C=4.5$ meV for $B=10$ T. Equation (4) then yields $\hbar\omega_+\sim 9.5$ meV and $\hbar\omega_-\sim 2$ meV. As a result, the smaller energy separation $\hbar\omega_-$ is reduced still further by B and may not be resolvable given the finite energy broadening of the states, quenching the structure in the density of states and reducing the number of observed fine structure peaks in the $I(V,B)$ characteristics.

In order to lend further support to this mechanism of fine structure quenching, we have calculated numerically the density of states in the lateral potential due to both inhomogeneous strain shown in Figs. 3(b) and 3(c) and the magnetic field B by direct discretization of the Schrödinger equation. With the in-plane heavy-hole effective mass $m^*=0.26m_0$, corresponding to the averaged strain $\varepsilon=-0.4$ in the quantum well, the calculated discrete state spectrum in $B=0$ and 10 T with no broadening is shown in Figs. 7(a) and 7(b) (here again, the reference zero of energy is the Fermi Level E_F in the emitter, consistent with Fig. 4). However, the scattering-limited lifetime imposes an energy broadening (there is also thermal broadening, which can be neglected at $T=1.7$ K). The lower two curves in Fig. 7(c) show the calculated densities of states for $B=0$ and 10 T with Gaussian broadening $\Gamma=\hbar/\tau=1.5$ meV, corresponding to a mobility $\mu=e\tau/m^*$ ~ 3000 cm^2/V s. This value is reasonable, given measured 2D hole gas mobilities in strained Si$_x$Ge$_{1-x}$ channels at low T in the 10^3-10^4 cm^2/V s range,[25,26] as well as recent calcula-

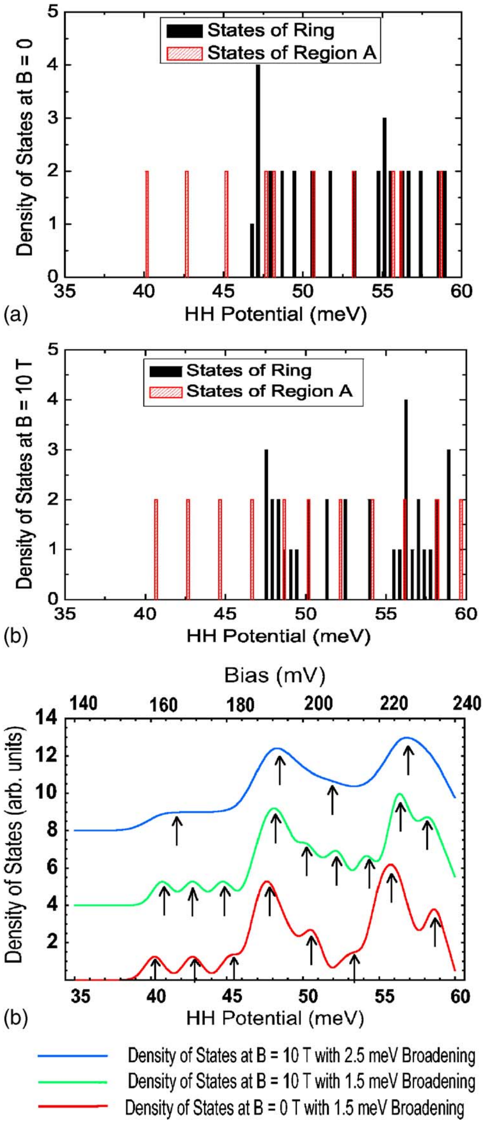

FIG. 7. (Color online) Numerically calculated HH densities of states in the elliptical quantum dot assuming no energy broadening at $B=$(a) 0 and (b) 10 T. States originating in the minimum potential regions A and the higher-lying ringlike regions B are indicated separately. (c) The same densities of states calculated with $\Gamma=1.5$ meV Gaussian energy broadening for $B=0$ and 10 T (lower curves), as well as the $B=10$ T density of states with a larger $\Gamma=2.5$ meV energy broadening (top curve). The energy scale is converted to applied bias at the top of (c) to facilitate direct comparison with the experimental $I(V)$ data of Fig. 5(a).

tions of hole mobility in strained Si_xGe_{1-x} channels with low carrier densities at low temperatures.[27] We find that as long as the broadening is unchanged by B, the number of peaks in the density of states is unchanged for our parameters, but some of the peaks are weakened and shifted toward each other in energy. However, if the energy broadening increases with B, consistent with the increased broadening of Landau levels in 2D carrier gases, the structure in the density of states can be partially quenched. Typically, the Gaussian broadening of Landau levels in 2D is predicted to increase as $B^{1/2}:\Gamma \sim (2\pi l_B{}^2)^{-1/2} = (eB/2\pi\hbar)^{1/2}$.[28,29] Thus, the top curve in Fig. 7(c) shows the density of states in the dot at $B = 10$ T, assuming increased broadening $\Gamma = 2.5$ meV. The number of peaks in the density of states and hence the number of fine structure peaks in the $I(V,B)$ is quenched, in qualitative agreement with the experimental data of Fig. 5(a). Clearly, the large number of simplifying assumptions employed in converting the inhomogeneous strain to an effective lateral potential, analysis in terms of analytically tractable parabolic potentials, as well as our use of a constant in-plane effective mass m^* at an averaged strain to estimate energy levels, precludes a quantitative comparison between the calculated density of states with experimental fine structure on the $I(V,B)$ characteristics.

VI. CONCLUSIONS

In summary, we use magnetotunneling spectroscopy to probe the hole states of the potential profile induced by the lateral inhomogeneous strain relaxation in a sub-100-nm elliptical quantum dot etched from a p-$Si/Si_{0.75}Ge_{0.25}$ double-barrier RT heterostructure. The resonant current peaks corresponding to tunneling into the heavy-hole and light-hole subbands in large devices develop quasiperiodic fine structure in our sub-100-nm elliptical quantum dot. The fine structure is partially quenched by high magnetic field B parallel to the current direction. We attribute the fine structure to the confined states in the quantum dot in the presence of both inhomogeneous strain and the magnetic field. Our experimental observations are consistent with our finite-element simulation of the potential induced by the strain relaxation and numerical calculations of density of states with and without magnetic field.

ACKNOWLEDGMENTS

The work at Brown has been funded by the NSF MRSEC (Grant No. DMR-0079964) and the NSF (Grants No. DMR-0302222, No. CMS-0093714, and No. CMS-0210095). The fabrication facilities are also supported in part by the Brown MRSEC.

---

[1] M. A. Reed, J. N. Randall, R. J. Aggarwal, R. J. Matyi, T. M. Moore, and A. E. Wetsel, Phys. Rev. Lett. **60**, 535 (1988).

[2] Bo Su, V. J. Goldman, and J. E. Cunningham, Phys. Rev. B **46**, 7644 (1992).

[3] S. Tarucha, D. G. Austing, Y. Tokura, W. G. van der Wiel, and L. P. Kouwenhoven, Phys. Rev. Lett. **84**, 2485 (2000).

[4] J. C. Bean, L. C. Feldman, A. T. Fiory, S. Nakahara, and I. K. Robinson, J. Vac. Sci. Technol. A **2**, 436 (1984).

[5] R. People, Phys. Rev. B **32**, 1405 (1985).

[6] A. A. Darhuber, T. Grill, J. Stangl, G. Bauer, D. J. Lockwood, J. P. Noel, P. D. Wang, and C. M. Sotomayor Torres, Phys. Rev. B **58**, 4825 (1998).

[7] A. Zaslavsky, K. R. Milkove, Y. H. Lee, B. Ferland, and T. O. Sedgwick, Appl. Phys. Lett. **67**, 3921 (1995).

[8] C. D. Akyuz, A. Zaslavsky, L. B. Freund, D. A. Syphers, and T. O. Sedgwick, Appl. Phys. Lett. **72**, 1739 (1998).

[9] P. W. Lukey, J. Caro, T. Zijlstra, E. Van der Drift, and S. Radelaar, Phys. Rev. B **57**, 7132 (1998).

[10] H. T. Johnson, L. B. Freund, C. D. Akyuz, and A. Zaslavsky, J. Appl. Phys. **84**, 3714 (1998).

[11] Jun Liu, A. Zaslavsky, and L. B. Freund, Phys. Rev. Lett. **89**, 096804 (2002).

[12] H. C. Liu, D. Landheer, M. Buchanan, and D. C. Houghton, Appl. Phys. Lett. **52**, 1809 (1988).

[13] V. J. Goldman, D. C. Tsui, and J. E. Cunningham, Phys. Rev. B **35**, 9387 (1987).

[14] V. J. Goldman, D. C. Tsui, and J. E. Cunningham, Phys. Rev. Lett. **58**, 1256 (1987).

[15] S. Luryi, Appl. Phys. Lett. **47**, 490 (1985).

[16] R. Wessel and M. Altarelli, Phys. Rev. B **40**, 12457 (1989).

[17] T. Manku and A. Nathan, Phys. Rev. B **43**, 12634 (1991).

[18] J. P. Cheng, V. P. Kesan, D. A. Grutzmacher, T. O. Sedgwick, and J. A. Ott, Appl. Phys. Lett. **62**, 1522 (1993).

[19] The in-plane effective mass m^* of hole subbands in our coupled Si/Si_xGe_{1-x} single quantum well was calculated using the six-band Luttinger-Kohn model; see J. M. Luttinger and W. Kohn, Phys. Rev. **97**, 869 (1955).

[20] U. Gennser, V. P. Kesan, D. A. Syphers, T. P. Smith III, S. S. Iyer, and E. S. Yang, Phys. Rev. Lett. **67**, 3828 (1991).

[21] The calculations are carried out using the finite-element program ABAQUS.

[22] J. M. Luttinger and W. Kohn, Phys. Rev. **97**, 869 (1955); J. M. Luttinger, *ibid.* **102**, 1030 (1956).

[23] G. Ihm, M. L. Falk, S. K. Noh, S. J. Lee, and T. W. Kim, Phys. Rev. B **46**, 15270 (1992).

[24] N. Mori, P. H. Beton, J. Wang, and L. Eaves, Phys. Rev. B **51**, 1735 (1995).

[25] D. J. Paul, N. Griffin, D. D. Arnone, M. Pepper, C. J. Emeleus, P. J. Phillips, and T. E. Whall, Appl. Phys. Lett. **69**, 2704 (1996).

[26] M. A. Sadeghzadeh, A. I. Horrell, O. A. Mironov, E. H. C. Parker, T. E. Whall, and M. J. Kearney, Appl. Phys. Lett. **76**, 2568 (2000).

[27] D. N. Quang, V. N. Tuoc, T. D. Huan, and P. N. Phong, Phys. Rev. B **70**, 195336 (2004).

[28] G. Gobsch, D. Schulze, and G. Paasch, Phys. Rev. B **38**, 10943 (1988).

[29] T. Ando and Y. Uemura, J. Phys. Soc. Jpn. **36**, 959 (1974); R. R. Gerhardts, Z. Phys. B **21**, 275 (1975).